Interface engineering of phase separation in $SrRuO_3/SrTiO_3$ hybrid superlattices

Zhangzhang Cui,[1,2,*] Yingying Zhang,[3,†] Xiaofang Zhai,[4] Hanghui Chen,[5,6] Yi-De Chuang,[7] Jinghua Guo,[7] Zhengping Fu,[1,2] Zhengcao Li,[3] and Yalin Lu[1,2,‡]

[1]*Hefei National Research Center for Physical Sciences at the Microscale, and Department of Materials Science and Engineering, University of Science and Technology of China, Hefei, Anhui 230026, China*

[2]*Anhui Laboratory of Advanced Photon Science and Technology, University of Science and Technology of China, Hefei, Anhui 230026, China*

[3]*State Key Laboratory for New Ceramics and Fine Processing, Key Laboratory of Advanced Materials of Ministry of Education, School of Materials Science and Engineering, Tsinghua University, Beijing 100084, China*

[4]*School of Physical Science and Technology, ShanghaiTech University, Shanghai 201210, China*

[5]*NYU-ECNU Institute of Physics, NYU Shanghai, Shanghai 200122, China*

[6]*Department of Physics, New York University, New York, New York 10003, USA*

[7]*Advanced Light Source, Lawrence Berkeley National Laboratory, Berkeley, California 94720, USA*

(Received 14 June 2021; revised 27 June 2022; accepted 14 July 2022; published 27 July 2022)

Most observed phase separation phenomena in complex oxides occur in systems with chemical dopants or structural defects, and theories have established the strong connection between phase separation and the random distribution of chemical dopants. Recent experiments on fabricated high-quality oxide superlattices also confirmed that the phase separation is suppressed in the clean systems without chemical disorders. Thus far, phase separation in strongly correlated oxides without the need of chemical dopants or structural defects has not been fully demonstrated. Here, we have built chemically ordered hybrid superlattices using prototypical $SrRuO_3$ and $SrTiO_3$ perovskite oxides. Contrary to previous understandings, we observe phase separation of two magnetic phases with different spin easy axes. We elucidate this phenomenon through first-principles calculations that the hybrid superlattices have a spontaneous structural instability, leading to a coexistence of ferromagnetic and antiferromagnetic phases. Our findings provide an alternative pathway other than chemical doping to introduce phase separation in correlated oxides and imply that phase separation can exist in clean systems without the need of chemical disorders.

DOI: 10.1103/PhysRevB.106.024424

I. INTRODUCTION

Phase separation in complex oxides is often manifested by the competition between multiple phases with distinct electronic/magnetic properties [1]. This phenomenon is most prominent in superconducting cuprates and colossal magnetoresistance manganites, which typically show the coexistence of metallic and insulating phases on the micrometer to nanometer length scales [2,3]. In most cases, phase separation phenomena are induced by chemical doping through ionic replacements, interstitials, or vacancies in the parent compounds [2–5]. Occasionally, phase separation appears in some oxides with no apparent chemical doping, such as $CaFe_3O_5$ and $LuFe_2O_4$; however, cation nonstoichiometry still exists in these oxides [6,7] such that they can be viewed as solid solutions of Fe^{2+} and Fe^{3+}. The chemical dopants inevitably distribute randomly in the lattice, leading to a quenched disorder, and the role of such randomness in phase transition has been one of the main research subjects in condensed-matter physics [8,9].

The effects of chemical doping or chemical disorders on phase separation in strongly correlated oxides have been extensively studied. In particular, oxygen doping is an indispensable way for inducing coexisting superconducting and antiferromagnetic insulating phases in La_2CuO_4 because oxygen dopants not only provide extra charges, the segregation of excess oxygen also helps compensate the long-range Coulomb repulsion [2,10]. Similar phenomenon also occurs at the interface of $LaAlO_3/SrTiO_3$ heterostructures where the coexistence of superconductivity and magnetic orders has been reported [11–14]. The selective occupancy of Ti d orbitals at the interface arising from the presence and nonuniform distribution of oxygen vacancies is believed to be the origin of the phase separation [15]. As for the colossal magnetoresistance systems where the ferromagnetic metallic and charge-ordered insulating phases coexist, the chemical dopants randomly modify the Mn–O–Mn bond angles and subsequently tune the bandwidth. The disorder of the dopants leads to a random electron hopping between nearby Mn ions as well as a random exchange interaction between the localized spins [3,16], and theories have predicted that the phase separation in manganites would be suppressed if fully chemically ordered structures could be achieved [17–20]. Remarkably, this prediction was confirmed in recent experiments in which tricolor manganite superlattices were fabricated using a layer-by-layer growth technique to exclude chemical disordering [21,22].

Thus far, the existence of phase separation in strongly correlated oxides without the presence of chemical disorders or structural defects has not been fully proved. This phase

*zzcui@ustc.edu.cn
†zyy2023@tsinghua.edu.cn
‡yllu@ustc.edu.cn

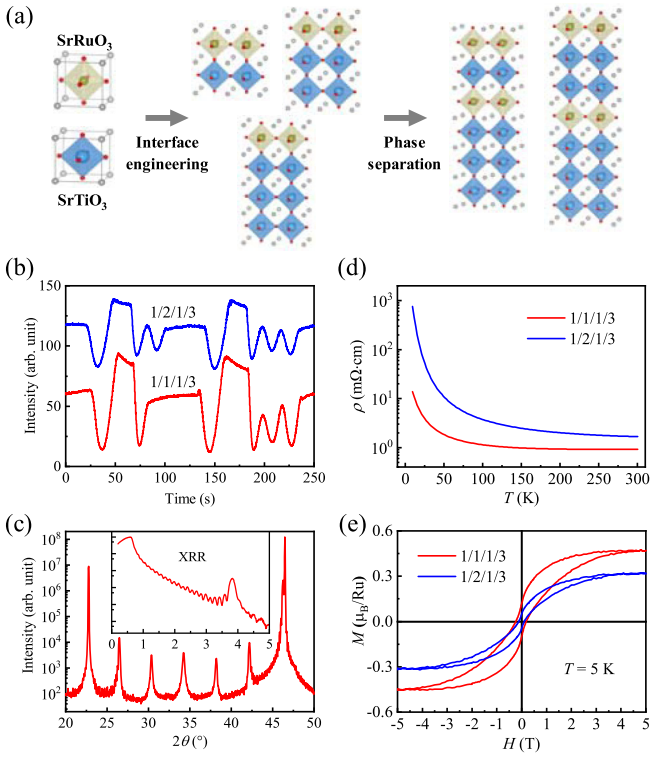

FIG. 1. (a) Schematics of the design of hybrid superlattices using perovskite blocks of pseudocubic SRO and STO unit cells. (b) RHEED intensity oscillations of 1/1/1/3 and 1/2/1/3 superlattices. (c) XRD ω-2θ scans of 1/1/1/3 superlattice. The inset shows the x-ray reflectivity (XRR) profile. (d) Temperature-dependent resistivity and (e) magnetic field-dependent out-of-plane magnetizations of 1/1/1/3 and 1/2/1/3 superlattices.

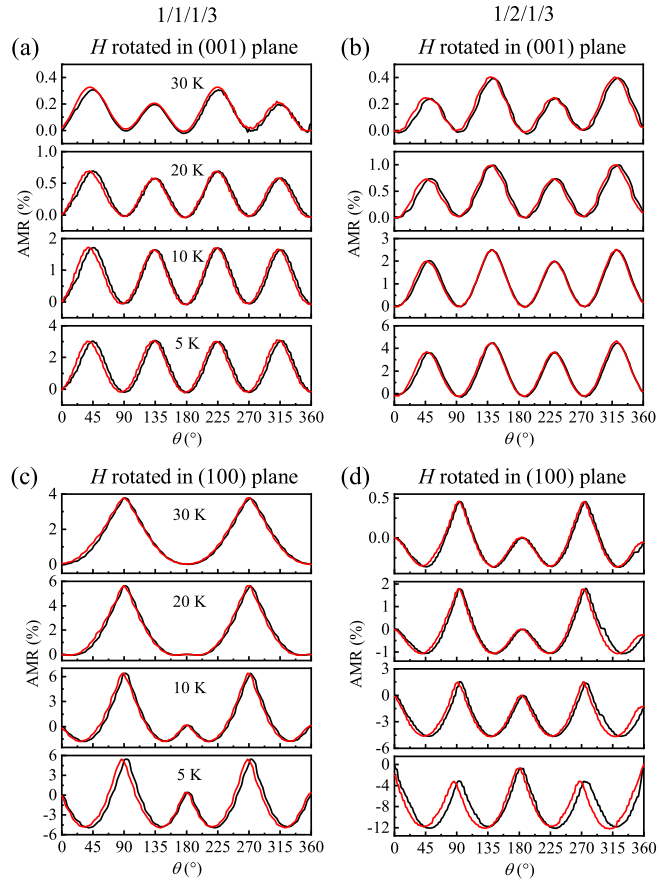

FIG. 2. AMRs of (a) 1/1/1/3 and (b) 1/2/1/3 superlattices measured at $T = 5$, 10, 20, and 30 K with $H = 9$ T rotated in the (001) plane. The electric current is driven along the [110] direction. Here, θ is the angle between H and the [110] direction. AMRs of (c) 1/1/1/3 and (d) 1/2/1/3 superlattices measured at $T = 5$, 10, 20, and 30 K with $H = 9$ T rotated in the (100) plane. The electric current is driven along the [100] direction, always perpendicular to H. Here, θ is the angle between H and the [001] direction. In all measurements, H is swept from 0° to 360° (black curves), and then back to 0° (red curves).

separation has far-reaching scientific and technological implications, for examples, reducing the power consumption in colossal magnetoresistive devices due to less electronic scattering by removing the dopants [22], and achieving an intrinsic coexistence of superconductivity and magnetism on the same electrons [23]. In this work, we design hybrid superlattices [see schematic illustration in Fig. 1(a)] through a layer-by-layer growth of the prototypical $SrRuO_3$ (SRO) and $SrTiO_3$ (STO) perovskite oxides. Experimentally, we observe a phase separation of two magnetic phases that have ⟨001⟩ and ⟨110⟩ magnetic easy axes, respectively. In addition, first-principles calculations show that this phenomenon is caused by the coexisting ferromagnetic metallic and antiferromagnetic insulating phases driven by the nonuniform distribution of the metal–oxygen bond angles. Our work provides an alternative other than chemical doping to introduce phase separation in complex oxides. More importantly, it demonstrates the potential to introduce phase separation in properly designed oxide superlattices with full chemical ordering.

II. RESULTS AND DISCUSSION

A. Structural, transport, and magnetic characterizations

The hybrid superlattices were epitaxially grown on (001)-oriented STO substrates using pulsed laser deposition (PLD) assisted by the *in situ* monitoring of reflective high-energy electron diffraction (RHEED) patterns. Specifically, $(SRO)_1/(STO)_1/(SRO)_1/(STO)_3$ (referred to as 1/1/1/3) is the combination of $(SRO)_1(STO)_1(1/1)$ and $(SRO)_1/(STO)_3$ (1/3) superlattices as schematically illustrated in Fig. 1(a). Similarly, $(SRO)_1/(STO)_2/(SRO)_1/(STO)_3$ (referred to as 1/2/1/3) is the combination of $(SRO)_1/(STO)_2$ (1/2) and 1/3 superlattices. As seen in Fig. 1(b), both the growth of SRO and STO layers exhibits clear RHEED intensity oscillations, displaying an excellent layer-by-layer epitaxy and precise single unit-cell level control. The total repetition of the supercells is 25 (or 50 SRO monolayers) for both superlattices. X-ray diffraction (XRD) ω-2θ scans of the superlattices are shown in Fig. 1(c) and Supplemental Material Fig. S1 [24]. The superlattices exhibit sharp diffraction peaks corresponding to the supercell structures as designed. The average out-of-plane lattice constant of a single perovskite layer in the superlattices is calculated to be ~3.92 Å. Figures 1(d) and 1(e) are the temperature (T)-dependent resistivity (ρ) and magnetic field (H)-dependent out-of-plane magnetizations (M) of the

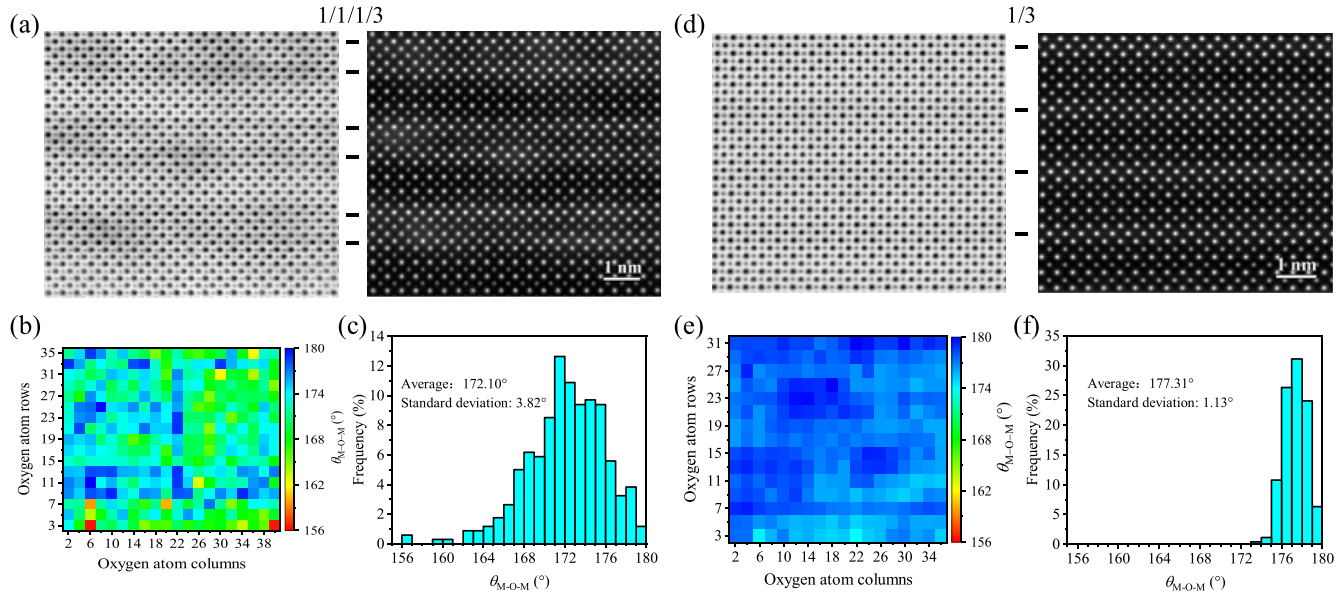

FIG. 3. ABF-STEM (left panel) and corresponding HAADF-STEM (right panel) images of (a) 1/1/1/3 and (d) 1/3 superlattices. The ABF and HAADF images are taken at the same area. The black markers indicate the positions of SRO layers. Map of metal–oxygen bond angle $\theta_{M\text{-}O\text{-}M}$ as a function of oxygen positions of (b) 1/1/1/3 and (e) 1/3 superlattices. Statistical histogram of $\theta_{M\text{-}O\text{-}M}$ of (c) 1/1/1/3 and (f) 1/3 superlattices.

superlattices, respectively. Both superlattices display a semiconducting transport behavior and weak ferromagnetism.

B. Anisotropic magnetoresistance measurements

Anisotropic magnetoresistance (AMR) is a magnetotransport counterpart of magnetocrystalline anisotropy energy (MAE), which has been widely utilized to investigate the magnetic anisotropy of magnetic materials [25–28]. The normal AMR effect is caused by the spin-orbit coupling (SOC) that mixes spin-up and spin-down states [29–31] and the resistance simply depends on the angle between the magnetization and the electric current; hence, a twofold dependence of the AMR is expected [29]. The MAE can also give rise to a remarkable magnetoresistance that depends on the spin orientations with respect to the crystalline axes, which is caused by the spin-dependent scattering of transport electrons [25,26,32]. Figure 2 shows the AMRs of 1/1/1/3 and 1/2/1/3 superlattices measured over a broad temperature range. The AMR measurement geometry is schematically shown in Supplemental Material Fig. S2 [24]. For convenience, pseudocubic indices of the superlattices are used throughout the paper. In Figs. 2(a) and 2(b), a 9-T magnetic field is rotated in the (001) plane and the electric current (I) is driven along the [110] direction. It can be clearly seen in these figures that the AMRs of both superlattices show a fourfold symmetry at $T = 5$–30 K. This fourfold symmetry cannot arise from the normal AMR effect and must be attributed to the MAE symmetry of the superlattices. It suggests that the magnetic easy axes in the (001) plane are along the fourfold ⟨110⟩ axes of SRO pseudocubic unit cell (u.c.).

Figures 2(c) and 2(d) are the AMRs of 1/1/1/3 and 1/2/1/3 superlattices in which the $H = 9$ T field is rotated in the (100) plane and I is driven along the [100] direction. In this measurement geometry, H is always perpendicular to I so that the normal AMR effect is excluded and only the magnetocrystalline component of the AMR is detected. Obviously, the AMRs of both superlattices do not show the standard fourfold symmetry. For the 1/1/1/3 superlattice, at $T = 20$ and 30 K the AMR has a nearly standard twofold symmetry with peaks at $\theta = 90°/270°$, in agreement with a perpendicular magnetic anisotropy with ⟨001⟩ easy axis. With decreasing temperature, at $T = 5$ and 10 K additional peaks appear at $\theta = 0°/180°$ in the AMR. Similarly, for the 1/2/1/3 superlattice, the AMRs at $T = 5$ and 10 K are close to a fourfold symmetry, while with increasing temperature an additional twofold AMR appears.

As comparisons, the AMRs of 1/1, 1/2, 2/4, and 1/3 superlattices are also measured (see Supplemental Material Figs. S3 and S4 [24]). The 1/1 and 2/4 superlattices show twofold AMRs while the 1/3 superlattice exhibits a fourfold AMR. And, the 1/2 superlattice has a coexistence of twofold and fourfold AMRs. The twofold AMR can be attributed to a perpendicular magnetic anisotropy with ⟨001⟩ easy axis that is common in SRO heterostructures with itinerant ferromagnetism [33,34], while the fourfold AMR is unusual in SRO heterostructures, which has only been reported in the insulating $(SRO)_1/(STO)_N$ superlattices in our previous work and was attributed to eightfold ⟨111⟩ easy axes [35]. The AMR measurement of 1/1/1/3 and 1/2/1/3 superlattices indicates a coexistence of a magnetic phase with ⟨001⟩ easy axis and another phase with ⟨110⟩ easy axes in the (001) plane.

C. Scanning transmission electron microscopy

To reveal how the phase separation of the two magnetic phases with different magnetic anisotropies emerges, we perform detailed atomically resolved cross-sectional aberration-corrected scanning transmission electron microscopy (STEM) measurements on the 1/1/1/3 and 1/3 superlattices, as shown

in Fig. 3. Clear interfaces between SRO and STO are visible in the high-angle annular dark-field (HAADF) STEM images [see right panels in Figs. 3(a) and 3(d)], suggesting a good chemical ordering of Ru and Ti atoms across the superlattices. The positions of the oxygen and metal atom columns are extracted from the annular bright-field (ABF) STEM images [see left panels in Figs. 3(a) and 3(d)]. We then map the out-of-plane metal–oxygen bond angle ($\theta_{\text{M-O-M}}$, M = Ru or Ti) as a function of oxygen positions [see Figs. 3(b) and 3(e)]. The statistics of $\theta_{\text{M-O-M}}$ is summarized in Figs. 3(c) and 3(f). It shows that $\theta_{\text{M-O-M}}$ of 1/1/1/3 superlattice has quite a wide dispersion from 156° to 180°. Such a large $\theta_{\text{M-O-M}}$ dispersion is unusual, unprecedented in most transition-metal perovskite-oxide heterostructures [36–39]. On the contrary, the $\theta_{\text{M-O-M}}$ of 1/3 superlattice exhibits a much narrower dispersion. It is known that bulk STO has no out-of-plane oxygen octahedral tilt [40,41], while bulk SRO has a $\theta_{\text{Ru-O-Ru}}$ around 168° [36]. The abrupt discontinuity between the tilts of TiO_6 and RuO_6 octahedra would cause a structural instability and nonuniform distribution of $\theta_{\text{M-O-M}}$ in the superlattices.

D. First-principles calculations

The bandwidth and conductivity of the superlattices are mainly determined by the electron hopping between adjacent SRO monolayers, as schematically shown in Fig. 4(a). The STO layer thickness and the metal–oxygen bond angle $\theta_{\text{M-O-M}}$ are the main parameters to control the hopping amplitude. To investigate how the nonuniform distribution of $\theta_{\text{M-O-M}}$ influence the electronic and magnetic properties, we perform first-principles calculations on the 1/1/1/3 superlattice. First, we start from the crystal structure with $a^0a^0c^-$ ($\alpha = \beta = 0°$, $\gamma = 5°$, space group $P4/mbm$) oxygen octahedral rotation such that the out-of-plane $\theta_{\text{M-O-M}}$ is constrained to 180°. During the atomic relaxation, the crystal symmetry is kept unchanged while the atomic positions and in-plane bond angles are optimized. In the density-functional theory plus Hubbard U (DFT+U) calculation, both ferromagnetic (FM) and antiferromagnetic (AFM, including A-, C-, and G-type spin alignments) states are considered. The FM alignment is the ground state and has a metallic band structure [see the near Fermi-level density of states (DOS) in Fig. 4(b)]. We then turn on SOC to study the magnetic anisotropy and find the ⟨001⟩ orientation has the lowest energy among the four calculated orientations of Ru magnetic moment, as shown in Fig. 4(c).

Then we perform the same calculation on the crystal structure with $a^-a^-c^-$ ($\alpha = \beta = 8°$, $\gamma = 12°$, space group $P2_1/c$) rotation such that the out-of-plane $\theta_{\text{M-O-M}}$ is originally set as a uniform value less than 180°. During the atomic relaxation, the crystal symmetry is kept unchanged while both the in-plane and out-of-plane bond angles are allowed to relax. It is interesting that after atomic relaxation, $\theta_{\text{M-O-M}}$ is no longer uniform but shows a remarkable dispersion [see Fig. 4(d)]. This result is quite different from previous calculations on 1/1 and 1/3 superlattices that show uniform oxygen octahedral tilts [35,39]. It should be noted that though the calculated standard deviation of $\theta_{\text{M-O-M}}$ is smaller than the experimental value of 3.82°, the DFT calculations successfully capture the key feature, i.e., the structural instability of 1/1/1/3 hybrid

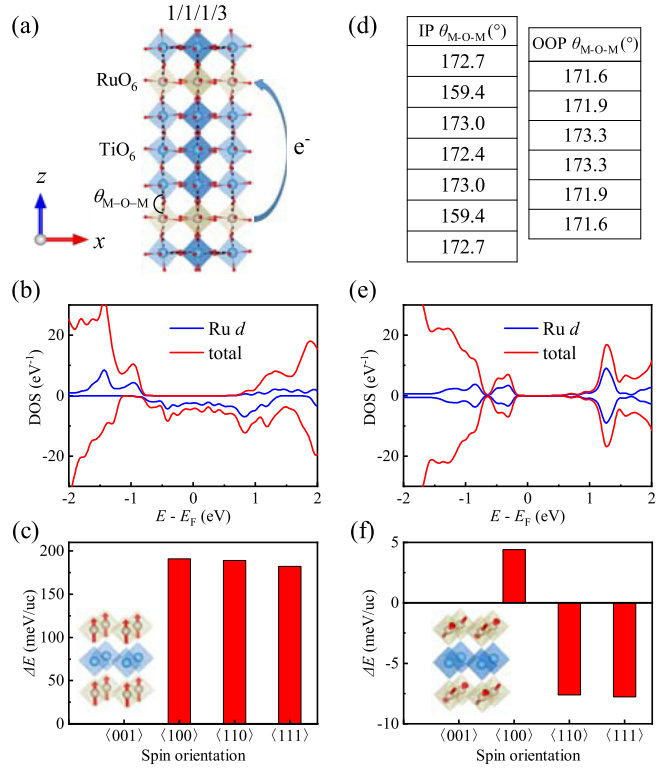

FIG. 4. (a) Schematic of the unit cell of 1/1/1/3 superlattice used in the first-principles calculations. The dashed lines indicate the volume of a single unit cell. (b) Near Fermi-level DOS and (c) total energies with different Ru magnetic moment orientations of 1/1/1/3 superlattice calculated on $a^0a^0c^-$ crystal structure. (d) Layer-dependent in-plane (IP) and out-of-plane (OOP) metal–oxygen bond angles, (e) near Fermi-level DOS, and (f) total energies with different Ru magnetic moment orientations of 1/1/1/3 superlattice calculated on $a^-a^-c^-$ crystal structure. (b), (e) The states in the upper (lower) half correspond to spin up (down). (c), (f) The energy of the ⟨001⟩ state is used as the reference. The FM spin alignment with ⟨001⟩ magnetic anisotropy is schematically shown in the inset of (c). And, the G-type AFM spin alignment with ⟨111⟩ magnetic anisotropy is schematically shown in the inset of (f).

superlattice that is not present in the 1/1 and 1/3 superlattices. Moreover, the DFT+U calculation finds the G-type AFM insulating state has the lowest energy (C-type AFM alignment is only ∼0.06 meV/u.c. higher) [see the near Fermi-level DOS in Fig. 4(e)]. After including SOC, it turns out that the magnetic easy axis changes to the ⟨111⟩ direction [see Fig. 4(f)]. We also realize that the total energies with Ru spin orientation in ⟨110⟩ and ⟨111⟩ directions are very close, ∼0.16 meV/u.c. in difference. Both spin alignments will give rise to a fourfold AMR in the (001) plane.

For comparison, we further perform a similar calculation on a 1/2/1/2 superlattice (see Supplemental Material Fig. S10 [24]). The DFT calculation again finds the superlattice has nonuniform bond angles. And, the superlattice with $a^0a^0c^-$ and $a^-a^-c^-$ oxygen octahedral rotations also has FM metallic and AFM insulating ground states, respectively, in agreement with the AMR measurements of 1/2 superlattice (see Supplemental Material Fig. S4 [24]). Whereas, different from the 1/1/1/3 hybrid superlattice, the bond angles

of 1/2/1/2 sample are less dispersed, indicating that the structural instability can be enhanced by the asymmetric superlattice structure, in consistency with the observation that at the same measuring temperature of 5 K, the 1/2 superlattice shows a pure fourfold AMR while the 1/1/1/3 exhibits a coexistence of twofold and fourfold AMRs.

III. CONCLUSIONS

The calculated electronic properties, magnetic anisotropies, and $\theta_{\text{M-O-M}}$ distributions of the superlattices are in good agreement with the AMR and STEM results. It demonstrates that at proper Ru ratios, growth sequences, and SRO layer isolations, the SRO/STO superlattices will have a structural instability and nonuniform distribution of $\theta_{\text{M-O-M}}$. The structural instability can be further enhanced due to the asymmetric lattice structure of the hybrid superlattice. Large $\theta_{\text{M-O-M}}$ favors a FM metallic state while small $\theta_{\text{M-O-M}}$ stabilizes an AFM insulating state. It is precisely this factor that leads to the phase separation into FM and AFM states in the superlattices. The metallic-like phase could only account for few portions (inferred from the ABF-STEM results), so that the superlattices as a whole exhibit an insulating behavior. We have measured the resistivity and Hall coefficients of the superlattices that are also in consistency with this scenario (see Supplemental Material Fig. S11 [24]). Furthermore, it should be noted that chemical disorders such as oxygen vacancies and Ru/Ti intermixing could not be the main cause of the phase separation, because all the superlattices are prepared at exactly the same conditions while the phase separation is only observed in the 1/2, 1/1/1/3, and 1/2/1/3 superlattices, not seen in the 1/1, 2/4, and 1/3 samples.

In summary, we have fabricated high-quality hybrid superlattices of prototypical SRO and STO perovskite oxides using the layer-by-layer growth technique. Different from previous theoretical and experimental studies on transition-metal oxides where chemical disorders are needed to induce phase separation, we have demonstrated the phase separation of two magnetic phases in the hybrid superlattices, one with ⟨001⟩ easy axis and the other with ⟨110⟩ easy axes in the (001) plane. We further elucidate through first-principles calculations that the observed phase separation originates from the coexisting FM and AFM states, caused by the spontaneous nonuniform distribution of metal–oxygen bond angles. Our work provides insights to one of the widely discussed topics in strongly correlated oxides of whether phase separation can exist in clean systems without the need of chemical disorders. Besides, our results provide another way other than chemical doping to introduce phase separation in complex oxides, which is promising to develop exotic functionalities.

ACKNOWLEDGMENTS

This work supported by the National Natural Science Foundation of China (Grants No. 12004367 and No. 51627901), the National Key Research and Development Program of China, the Ministry of Science and Technology (Grants No. 2016YFA0401004, No. 2017YFA0402904, and No. 2019YFA0405604), and Anhui Initiative in Quantum Information Technologies (Grant No. AHY100000). Y.-D.C. and J.G. acknowledge the support of the Advanced Light Source, a U.S. DOE Office of Science User Facility, under Contract No. DE-AC02-05CH11231.

[1] S. W. Cheong, P. A. Sharma, N. Hur, Y. Horibe, and C. H. Chen, Physica B **318**, 39 (2002).
[2] E. Sigmund and K. A. Müller, *Phase Separation in Cuprate Superconductors* (Springer-Verlag, Heidelberg, 1994).
[3] E. Dagotto, T. Hotta, and A. Moreo, Phys. Rep. **344**, 1 (2001).
[4] Y. Drees, Z. W. Li, A. Ricci, M. Rotter, W. Schmidt, D. Lamago, O. Sobolev, U. Rutt, O. Gutowski, M. Sprung, A. Piovano, J. P. Castellan, and A. C. Komarek, Nat. Commun. **5**, 5731 (2014).
[5] T. H. Kim, M. Angst, B. Hu, R. Jin, X. G. Zhang, J. F. Wendelken, E. W. Plummer, and A. P. Li, Proc. Natl. Acad. Sci. USA **107**, 5272 (2010).
[6] K. H. Hong, A. M. Arevalo-Lopez, J. Cumby, C. Ritter, and J. P. Attfield, Nat. Commun. **9**, 2975 (2018).
[7] J. Bourgeois, G. André, S. Petit, J. Robert, M. Poienar, J. Rouquette, E. Elkaïm, M. Hervieu, A. Maignan, C. Martin, and F. Damay, Phys. Rev. B **86**, 024413 (2012).
[8] Y. Imry and S.-K. Ma, Phys. Rev. Lett. **35**, 1399 (1975).
[9] T. Vojta, J. Phys. A: Math. Gen. **39**, R143 (2006).
[10] J. D. Jorgensen, B. Dabrowski, S. Pei, D. G. Hinks, L. Soderholm, B. Morosin, J. E. Schirber, E. L. Venturini, and D. S. Ginley, Phys. Rev. B **38**, 11337 (1988).
[11] L. Li, C. Richter, J. Mannhart, and R. C. Ashoori, Nat. Phys. **7**, 762 (2011).
[12] D. A. Dikin, M. Mehta, C. W. Bark, C. M. Folkman, C. B. Eom, and V. Chandrasekhar, Phys. Rev. Lett. **107**, 056802 (2011).
[13] J. A. Bert, B. Kalisky, C. Bell, M. Kim, Y. Hikita, H. Y. Hwang, and K. A. Moler, Nat. Phys. **7**, 767 (2011).
[14] X. Wang Ariando, G. Baskaran, Z. Q. Liu, J. Huijben, J. B. Yi, A. Annadi, A. R. Barman, A. Rusydi, S. Dhar, Y. P. Feng, J. Ding, H. Hilgenkamp, and T. Venkatesan, Nat. Commun. **2**, 188 (2011).
[15] V. N. Strocov, A. Chikina, M. Caputo, M. A. Husanu, F. Bisti, D. Bracher, T. Schmitt, F. Miletto Granozio, C. A. F. Vaz, and F. Lechermann, Phys. Rev. Mater. **3**, 106001 (2019).
[16] Y. Tomioka and Y. Tokura, Phys. Rev. B **70**, 014432 (2004).
[17] A. Moreo, M. Mayr, A. Feiguin, S. Yunoki, and E. Dagotto, Phys. Rev. Lett. **84**, 5568 (2000).
[18] J. Burgy, M. Mayr, V. Martin-Mayor, A. Moreo, and E. Dagotto, Phys. Rev. Lett. **87**, 277202 (2001).
[19] C. Sen, G. Alvarez, and E. Dagotto, Phys. Rev. B **70**, 064428 (2004).
[20] C. Sen, G. Alvarez, and E. Dagotto, Phys. Rev. Lett. **98**, 127202 (2007).
[21] T. Miao, L. Deng, W. Yang, J. Ni, C. Zheng, J. Etheridge, S. Wang, H. Liu, H. Lin, Y. Yu, Q. Shi, P. Cai, Y. Zhu, T. Yang, X. Zhang, X. Gao, C. Xi, M. Tian, X. Wu, H. Xiang, E. Dagotto, L. Yin, and J. Shen, Proc. Natl. Acad. Sci. USA **117**, 7090 (2020).
[22] Y. Zhu, K. Du, J. Niu, L. Lin, W. Wei, H. Liu, H. Lin, K. Zhang, T. Yang, Y. Kou, J. Shao, X. Gao, X. Xu, X. Wu, S. Dong, L. Yin, and J. Shen, Nat. Commun. **7**, 11260 (2016).

[23] S. S. Saxena, P. Agarwal, K. Ahilan, F. M. Grosche, R. K. W. Haselwimmer, M. J. Steiner, E. Pugh, I. R. Walker, S. R. Julian, P. Monthoux, G. G. Lonzarich, A. Huxley, I. Sheikin, D. Braithwaite, and J. Flouquet, Nature (London) **406**, 587 (2000).

[24] See Supplemental Material at http://link.aps.org/supplemental/10.1103/PhysRevB.106.024424 for details on methods and additional data of structural characterizations, transport measurements, and first-principles calculations, which includes Refs. [35,42–48].

[25] C. Lu, B. Gao, H. Wang, W. Wang, S. Yuan, S. Dong, and J.-M. Liu, Adv. Funct. Mater. **28**, 1706589 (2018).

[26] H. Wang, C. Lu, J. Chen, Y. Liu, S. L. Yuan, S.-W. Cheong, S. Dong, and J.-M. Liu, Nat. Commun. **10**, 2280 (2019).

[27] I. Fina, X. Marti, D. Yi, J. Liu, J. H. Chu, C. Rayan-Serrao, S. Suresha, A. B. Shick, J. Zelezny, T. Jungwirth, J. Fontcuberta, and R. Ramesh, Nat. Commun. **5**, 4671 (2014).

[28] D. Yi, J. Liu, S. L. Hsu, L. Zhang, Y. Choi, J. W. Kim, Z. Chen, J. D. Clarkson, C. R. Serrao, E. Arenholz, P. J. Ryan, H. Xu, R. J. Birgeneau, and R. Ramesh, Proc. Natl. Acad. Sci. USA **113**, 6397 (2016).

[29] E. D. Dahlberg, K. Riggs, and G. A. Prinz, J. Appl. Phys. **63**, 4270 (1988).

[30] A. P. Malozemoff, Phys. Rev. B **32**, 6080 (1985).

[31] R. Ramos, S. K. Arora, and I. V. Shvets, Phys. Rev. B **78**, 214402 (2008).

[32] P. Li, E. Y. Jiang, and H. L. Bai, Appl. Phys. Lett. **96**, 092502 (2010).

[33] W. Lu, P. Yang, W. D. Song, G. M. Chow, and J. S. Chen, Phys. Rev. B **88**, 214115 (2013).

[34] M. Ziese, I. Vrejoiu, and D. Hesse, Phys. Rev. B **81**, 184418 (2010).

[35] Z. Cui, A. J. Grutter, H. Zhou, H. Cao, Y. Dong, D. A. Gilbert, J. Wang, Y.-S. Liu, J. Ma, Z. Hu, J. Guo, J. Xia, B. J. Kirby, P. Shafer, E. Arenholz, H. Chen, X. Zhai, and Y. Lu, Sci. Adv. **6**, eaay0114 (2020).

[36] D. Kan, R. Aso, R. Sato, M. Haruta, H. Kurata, and Y. Shimakawa, Nat. Mater. **15**, 432 (2016).

[37] Z. Liao, M. Huijben, Z. Zhong, N. Gauquelin, S. Macke, R. J. Green, S. Van Aert, J. Verbeeck, G. Van Tendeloo, K. Held, G. A. Sawatzky, G. Koster, and G. Rijnders, Nat. Mater. **15**, 425 (2016).

[38] M. Saghayezhian, Z. Wang, H. Guo, R. Jin, Y. Zhu, J. Zhang, and E. W. Plummer, Phys. Rev. Res. **1**, 033160 (2019).

[39] M. Gu, Q. Xie, X. Shen, R. Xie, J. Wang, G. Tang, D. Wu, G. P. Zhang, and X. S. Wu, Phys. Rev. Lett. **109**, 157003 (2012).

[40] H. Vogt, Phys. Rev. B **51**, 8046 (1995).

[41] G. Shirane and Y. Yamada, Phys. Rev. **177**, 858 (1969).

[42] G. Kresse and J. Furthmuller, Comput. Mater. Sci. **6**, 15 (1996).

[43] J. P. Perdew, K. Burke, and M. Ernzerhof, Phys. Rev. Lett. **77**, 3865 (1996).

[44] S. L. Dudarev, G. A. Botton, S. Y. Savrasov, C. J. Humphreys, and A. P. Sutton, Phys. Rev. B **57**, 1505 (1998).

[45] M. Verissimo-Alves, P. Garcia-Fernandez, D. I. Bilc, P. Ghosez, and J. Junquera, Phys. Rev. Lett. **108**, 107003 (2012).

[46] R. Scherwitzl, S. Gariglio, M. Gabay, P. Zubko, M. Gibert, and J. M. Triscone, Phys. Rev. Lett. **106**, 246403 (2011).

[47] D. J. Groenendijk, N. Manca, J. de Bruijckere, A. Monteiro, R. Gaudenzi, H. S. J. van der Zant, and A. D. Caviglia, Eur. Phys. J. Plus **135**, 627 (2020).

[48] G. Herranz, B. Martínez, J. Fontcuberta, F. Sánchez, C. Ferrater, M. V. García-Cuenca, and M. Varela, Phys. Rev. B **67**, 174423 (2003).